

## Tropical Indian Ocean Variability in the IPCC Twentieth-Century Climate Simulations\*

N. H. SAJI AND S.-P. XIE

*IPRC, University of Hawaii at Manoa, Honolulu, Hawaii*

T. YAMAGATA

*University of Tokyo and FRSGC, Tokyo, Japan*

(Manuscript received 6 June 2005, in final form 13 December 2005)

### ABSTRACT

The twentieth-century simulations using by 17 coupled ocean–atmosphere general circulation models (CGCMs) submitted to the Intergovernmental Panel on Climate Change’s Fourth Assessment Report (IPCC AR4) are evaluated for their skill in reproducing the observed modes of Indian Ocean (IO) climate variability. Most models successfully capture the IO’s delayed, basinwide warming response a few months after El Niño–Southern Oscillation (ENSO) peaks in the Pacific. ENSO’s oceanic teleconnection into the IO, by coastal waves through the Indonesian archipelago, is poorly simulated in these models, with significant shifts in the turning latitude of radiating Rossby waves. In observations, ENSO forces, by the atmospheric bridge mechanism, strong ocean Rossby waves that induce anomalies of SST, atmospheric convection, and tropical cyclones in a thermocline dome over the southwestern tropical IO. While the southwestern IO thermocline dome is simulated in nearly all of the models, this ocean Rossby wave response to ENSO is present only in a few of the models examined, suggesting difficulties in simulating ENSO’s teleconnection in surface wind.

A majority of the models display an equatorial zonal mode of the Bjerknes feedback with spatial structures and seasonality similar to the Indian Ocean dipole (IOD) in observations. This success appears to be due to their skills in simulating the mean state of the equatorial IO. Corroborating the role of the Bjerknes feedback in the IOD, the thermocline depth, SST, precipitation, and zonal wind are mutually positively correlated in these models, as in observations. The IOD–ENSO correlation during boreal fall ranges from  $-0.43$  to  $0.74$  in the different models, suggesting that ENSO is one, but not the only, trigger for the IOD.

### 1. Introduction

Being part of a large warm water pool and neighboring the great monsoons of Asia that anchor the major convection center of the atmosphere, the Indian Ocean exerts climatic influences of global reach. There is growing evidence that its sea surface temperature (SST) changes play a key role in shaping important features of twentieth-century climate variability, from the drying trend of the African Sahel (Giannini et al.

2003) to the Pacific decadal variability (Deser et al. 2004) to the North Atlantic Oscillation (Hoerling et al. 2004). Recent model studies suggest that Indian Ocean SST modulates atmospheric convection and circulation, exerting a significant influence on the El Niño–Southern Oscillation (ENSO) (Yu et al. 2002; Wu and Kirtman 2004; Annamalai et al. 2005). The present study examines twentieth-century simulations by 17 coupled ocean–atmosphere general circulation models (CGCMs) submitted to the Intergovernmental Panel on Climate Change (IPCC) Fourth Assessment Report (AR4), focusing on their simulations of modes of interannual variability in Indian Ocean climate.

It is a quite challenging task for CGCMs to simulate Indian Ocean SST variability and its associated climate impacts because of a multitude of factors shaping SST variability in the region. While ENSO—an internal mode of ocean–atmosphere interaction—dominates tropical Pacific SST variance, the monsoons, ENSO,

---

\* International Pacific Research Center Contribution Number 362 and School of Ocean and Earth Science and Technology Contribution Number 6708.

---

Corresponding author address: N. H. Saji, International Pacific Research Center, 2525 Correa Rd., University of Hawaii at Manoa, Honolulu, HI 96822.  
E-mail: saji@hawaii.edu

and internal air–sea processes all have an important role to play in shaping Indian Ocean variability. For instance, a strong monsoon is followed by cooler than normal SSTs in the Arabian Sea. SST anomalies of a similar magnitude can also be created by teleconnection processes associated with ENSO. The Indian Ocean Dipole (IOD), a pattern of coupled ocean–atmosphere interaction, is yet another source of SST variance that modulates zonal SST gradients along the equator. The complexity is even increased as the elements discussed above interact among themselves. Further, the Indian Ocean warm pool is significantly affected by freshwater fluxes from a variety of sources including the Indonesian throughflow, heavy oceanic precipitation, and river runoff from adjacent land regions. This heightens the importance of mixed layer physics to ocean–atmospheric interaction (Perigaud and McCreary 2003; Qu and Meyers 2005). The representation of mixed layer physics, including thin low salinity layers and the barrier layers beneath, is possibly the most challenging aspect of modeling the Indian Ocean in climate models.

A successful simulation of Indian Ocean SST variability not only requires a successful simulation of the phenomena (both external and internal) that influence it, but also the processes that mediate between these and the SST anomalies. Consider the ENSO as an example. The ENSO is known to affect the Indian Ocean through three different teleconnection processes. One is an atmospheric teleconnection that modulates the thermodynamic fluxes at the sea surface (Klein et al. 1999; Yulaeva and Wallace 1994; Alexander et al. 2002), forcing basinwide SST anomalies following an ENSO event. The second process involves off-equatorial Rossby waves excited by ENSO-induced wind stress (Xie et al. 2002). The slow westward propagation of these Rossby waves prolongs the ENSO influence on Indian Ocean SSTs seasons after ENSO's demise. The third process involves the propagation of sea level anomalies from the western Pacific into the southeastern Indian Ocean (Clarke and Liu 1994; Wijffels and Meyers 2004), affecting SSTs there and consequently rainfall over northwestern Australia (Meyers 1996; England et al. 2006).

Indian Ocean SST anomalies, whether forced by external phenomena or developed internally through coupled processes, play a significant role in rainfall and temperature variability over the countries surrounding the Indian Ocean. It is well known that much of East African rainfall variability cannot be modeled without incorporating the effect of Indian Ocean SST anomalies (Goddard and Graham 1999; Latif et al. 1999). Over the southwest Indian Ocean, ENSO-induced ocean Rossby

waves affect local atmospheric convection and modulate tropical cyclone activity (Xie et al. (2002). SST anomalies associated with the IOD account for a significant fraction of rainfall variance over equatorial East Africa, Sri Lanka, Indonesia, and Australia (Ashok et al. 2001; Black et al. 2003; Lareef et al. 2003; Saji and Yamagata 2003a; Yamagata et al. 2004; Behera et al. 2005). Further, the IOD has a significant influence on subtropical surface air temperatures of both hemispheres through remote teleconnection processes (Saji and Yamagata 2003a; Saji et al. 2005a).

The present study evaluates the ability of climate models in simulating various aspects of SST variability in the Indian Ocean and the resultant impacts. To our knowledge, a systematic intercomparison of Indian Ocean variability among a large number of climate models has not been undertaken previously, an exercise that we believe will help clarify several outstanding issues concerning the genesis and nature of SST variability as well as the processes by which SST affects other climate variability in the Indian Ocean region. In particular we are interested in the processes by which ENSO is transmitted into the Indian Ocean, the role of ocean dynamics in the IOD, and the interaction between the IOD, ENSO, and monsoons. Specifically, we would like to address the following questions. Given that CGCMs have difficulty reproducing the mean states of the equatorial Pacific and Atlantic (Davey et al. 2002), how do they simulate mean Indian Ocean climate? Given that air–sea feedback and the thermocline feedback in particular appear important for observed IODs, does the thermocline depth in the eastern Indian Ocean control the IOD variance? Given that the IOD is significantly correlated with ENSO at the mature stage (September–November), do models with strong ENSO feature strong IOD–ENSO correlations? Another motivation for the present study is that a model intercomparison is essential to building confidence in modeled projections of future climate change in the Indian Ocean region.

The rest of the paper is organized as follows. Section 2 briefly describes the datasets. Section 3 compares model response to the ENSO, while section 4 examines the IOD in the simulations. Section 5 is a summary.

## 2. Data

Model simulations of SST, surface wind components, rainfall, and ocean subsurface temperatures were obtained for 17 CGCMs that submitted data for inclusion in the IPCC Fourth Assessment Report. Though 22 models had submitted their simulations, at the time of this analysis, we could extract all necessary data only

TABLE 1. Relation between model names, as used in the paper, and IPCC IDs.

Model	Institute	IPCC ID
CCMA_CGCM3_1 (M15)*	Canadian Centre for Climate Modelling and Analysis	CGCM3.1
CNRM_CM3 (M2)	Centre National de Recherches Météorologiques (France)	CNRM-CM3
CSIRO_MK3_O (M7)	CSIRO Atmospheric Research (Australia)	CSIRO-Mk3.0
GFDL_CM2_0 (M6)	Geophysical Fluid Dynamics Laboratory	GFDL-CM2.0
GFDL_CM2_1 (M3)	Geophysical Fluid Dynamics Laboratory	GFDL-CM2.1
GISS_AOM (M17)	Goddard Institute for Space Studies	GISS-AOM
GISSMODEL_E_H (M12)	Goddard Institute for Space Studies	GISS-EH
GISSMODEL_E_R (M16)	Goddard Institute for Space Studies	GISS-ER
UKMO_HADCM3 (M9)	Hadley Centre for Climate Prediction and Research	UKMO-HadCM3
IAP_FGOALS1_O_G (M1)	Institute of Atmospheric Physics (China)	FGOALS-g1.0
INMCM3 (M8)	Institute of Numerical Mathematic (Russia)	INM-CM3.0
IPSL_CM4 (M4)	Institut Pierre Simon Laplace (France)	IPSL-CM4
MIROC3_2_MEDRES (M13)	Center for Climate System Research (Japan)	MIROC3.2(medres)
MIROC3_2_HIRES (M14)	Center for Climate System Research	MIROC3.2(hires)
MRI_CGCM2_3_2A (M11)	Meteorological Research Institute (Japan)	MRI-CGCM2.3.2
NCAR_CCSM3_0 (M10)	National Center for Atmospheric Research	CCSM3
NCAR_PCM1 (M5)	National Center for Atmospheric Research	PCM

\* The string within parentheses denotes the respective label for the model in the figures.

for the 17 models listed in Table 1. In all of the following analysis, we have kept the original model resolutions, making no attempt to regrid the models to a single uniform resolution. Tables 1 and 2 give essential information on the models used in this study. Further detailed information can be obtained online ([http://www-pcmdi.llnl.gov/ipcc/model\\_documentation/ipcc\\_model\\_documentation](http://www-pcmdi.llnl.gov/ipcc/model_documentation/ipcc_model_documentation)). Most of the model runs are labeled by the name of the institution that performed the run and supplied the data. We refer to the models, according to the metadata information in the supplied data. These names are very similar to the suggested “IPCC IDs,” and we have mapped the relation between the two naming conventions in Table 1.

The set of simulations analyzed here is the so-called Climate of the Twentieth-Century Experiment (20c3M). The forcing agents of this experiment include greenhouse gases (CO<sub>2</sub>, CH<sub>4</sub>, N<sub>2</sub>O, and CFCs), sulfate aerosol direct effects, volcanoes, and solar forcing. The results reported in this analysis were based on runs whose external forcings were representative of the period between January 1900 and December 1999. The mean climatological annual cycle was defined using data for this whole period. Thereafter anomalies were found by subtracting the monthly mean variables from their respective climatological seasonal mean. To focus on the interannual part, we have also high-pass filtered the data using a Lanczos filter with 169 weights and a cutoff at 7 years. This cutoff was chosen both to reduce data loss at the end points and in consideration of the 2–7-yr periodicity of the ENSO signal.

The simulations were assessed against various observed and reanalyzed (assimilated) datasets. Atmo-

spheric surface winds were obtained from the European Centre for Medium-Range Weather Forecasts 40-yr reanalysis (ERA40), while oceanic three-dimensional temperatures were obtained from the Simple Ocean Data Assimilation (SODA) reanalysis (Carton et al. 2000). In addition, we used the observational datasets of Climate Prediction Center Merged Analysis of Precipitation (CMAP) (Xie and Arkin 1996) for rainfall and the Hadley Centre Global Sea Ice and Sea Surface Temperature (HISST) (Rayner et al. 2000) and Optimally Interpolated Sea Surface Temperature (OISST) (Reynolds and Smith 1994) for SST. Most of the observed–reanalysis datasets were available for the 45-yr period between January 1958 and December 2003, except for CMAP and OISST, which were available only after January 1979 and January 1982, respectively. High-pass filtering was not performed on the observations–reanalyses due to their shorter data length.

### 3. ENSO’s impact on Indian Ocean SST

The ENSO is a major force shaping Indian Ocean SST variability. Acting upon the ocean through different processes, the ENSO brings about three distinct patterns of SST anomalies in the Indian Ocean. As these patterns are important to local climate variability, we shall examine each of these in detail in the IPCC simulations. However, before we can proceed, we must establish the general character of ENSO in these models.

#### a. The Niño-3 index

Figure 1 shows the standard deviation of SST anomalies, averaged between 5°S and 5°N, as a function of

TABLE 2. Brief description of the coupled models used in this study.

Model	Resolution*		Flux adjustment**	Reference
	Atmosphere	Ocean		
CCCMA_CGCM3_1	3.75 × 3.75	1.85 × 1.85	None	Flato and Boer (2001)
CNRM_CM3	2.8 × 2.8	0.5 × 2.0	None	Salas-Melia et al. (2005, manuscript submitted to <i>Climate Dyn.</i> )
CSIRO_MK3_O	T63	0.84 × 1.875	None	Cai et al. (2005)
GFDL_CM2_0	2.0 × 2.5	0.33 × 1.0	None	Delworth et al. (2006)
GFDL_CM2_1	2.0 × 2.5	0.33 × 1.0	None	Delworth et al. (2006)
GISS_AOM	3 × 4	3 × 4	None	Russell et al. (1995)
GISSMODEL_E_H	4 × 5	2 × 2	None	Schmidt et al. (2006)
GISSMODEL_E_R	4 × 5	4 × 5	None	Schmidt et al. (2006)
UKMO_HADCM3	2.5 × 3.75	0.3 × 1.25	None	Gordon et al. (2000)
IAP_FGOALS1_O_G	2.8 × 2.8	1 × 1	None	Yu et al. (2004)
INMCM3	4 × 5	2.0 × 2.5	W	Diansky and Volodin (2002)
IPSL_CM4	2.5 × 3.75	1 × 2	None	Goosse and Fichefet (1999)
MIROC3_2_MEDRES	T42	0.5 × 1.4	None	Nozawa et al. (2005)
MIROC3_2_HIRES	T106	0.1875 × 0.28125	None	Nozawa et al. (2005)
MRI_CGCM2_3_2A	2.8 × 2.8	1.5 × 2.5	HWM	Yukimoto et al. (2001)
NCAR_CCSM3_0	T85	0.27 × 1.125	None	Kiehl and Gent (2004)
NCAR_PCM1	T42	0.27 × 1.125	None	Meehl et al. (2005)

\* Degrees latitude × longitude; resolution at the latitude closest to equator is shown.

\*\* H: heat; W: water; M: momentum.

calendar month and longitude. The top three panels show results from two different observational datasets and a reanalysis dataset. Except for OISST showing somewhat stronger amplitude compared to the others, the patterns of evolution are similar among the three. The larger amplitude in OISST is not related to its shorter and more recent record, but is likely a result of its better spatial and temporal sampling of satellite observations to the ship-based historical measurements in HISST.

On the other hand, the different climate models exhibit a larger spread in the simulated ENSO behavior. Only one of the models shown here (CNRM\_CM3) shows close resemblance in the spatiotemporal evolution (but nearly double the amplitude) relative to the observations–reanalysis. Other noteworthy discrepancies include a shift of the maximum in SST standard deviation to the western/central Pacific (e.g., INMCM3) and weaker/stronger amplitudes (e.g., MIROC3\_2\_HIRES/IAP\_FGOALS1\_O\_G). In one of the models (IAP\_FGOALS1\_O\_G), the eastward propagation of SST standard deviation is as pronounced as the westward propagation.

Given the differences in the equatorial SST variance distribution, one may question the use of a simple index such as Niño-3 (area-averaged SST between 5°S and 5°N, 150° and 90°W) to represent the ENSO variability in the climate model simulations. To address this issue, we calculated the time series for the first empirical orthogonal function (EOF) of wintertime (December–

February: DJF) tropical Pacific SST anomalies (25°S–25°N, 130°E–90°W). This is plotted against the Niño-3 index for DJF in Fig. 2. The close correspondence of both indices is likely due to the large spatial coherence of SST anomalies in the Pacific and suggests that, indeed, one may use the Niño-3 index to represent ENSO variability in the simulations. In the rest of the paper, the 17 models are enumerated in the order of their Niño-3 index variance, with M1 featuring the strongest ENSO variability. Models are referred to by number for convenience. The model corresponding to this number can be found in Fig. 3. For instance from Fig. 3, M12 = GISSMODEL\_E\_H. The left panel in Fig. 3 shows the month when the standard deviation of the Niño-3 time series peaks and the peak value. While in the majority of the models ENSO peaks in the November–January season, as in observations, several models feature an ENSO that peaks in July–August (M3, M5–M8, M10).

#### b. Thermodynamic influence of ENSO

A basinwide change in tropical Indian Ocean SSTs, which lags a season behind the ENSO, is one of the earliest known teleconnections of ENSO in the Indian Ocean (Pan and Oort 1983; Cadet 1985; Nigam and Shen 1993). Warmer SST anomalies in the Indian Ocean follow an El Niño and cooler ones a La Niña. The delayed basinwide SST pattern in the Indian Ocean appears to be primarily forced by surface heat flux anomalies remotely forced by SST anomalies in the

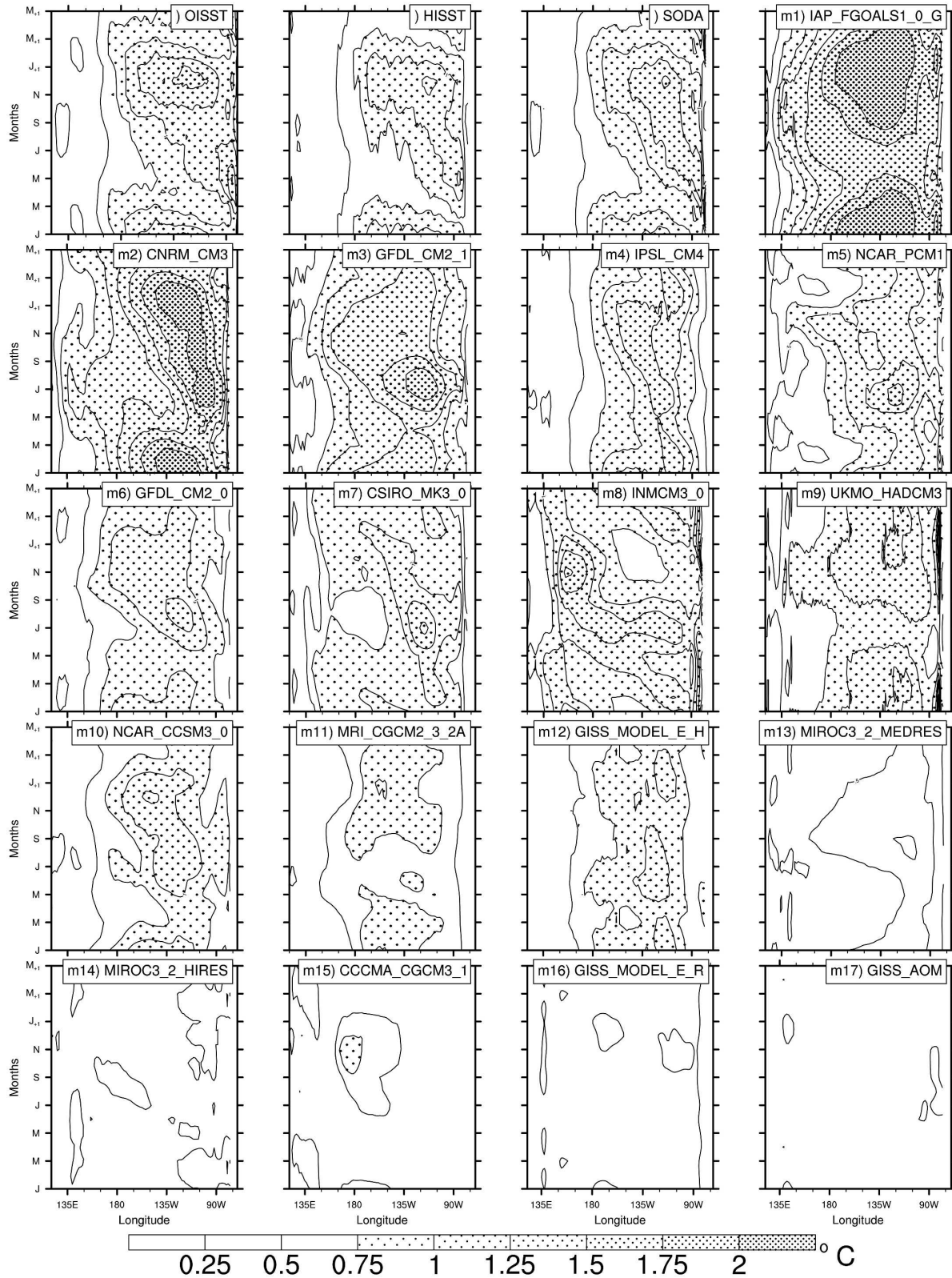


FIG. 1. Interannual standard deviation of equatorial Pacific SST anomalies (averaged from  $-5^{\circ}\text{S}$  to  $5^{\circ}\text{N}$ ) as a function of longitude and calendar month.

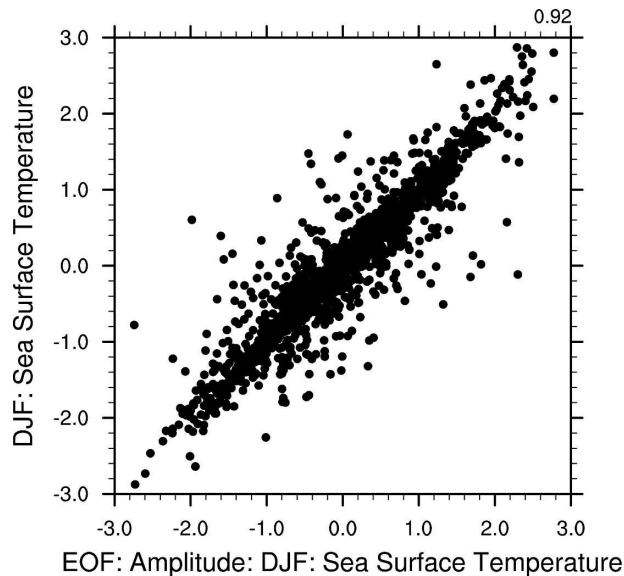


FIG. 2. Relationship between PC1 of the tropical Pacific SST and the Niño-3 index during DJF. All time series were normalized by their respective standard deviations. Simulations from all 17 CGCMs were pooled. The pooled correlation between PC1 and Niño-3 is 0.92.

equatorial eastern Pacific (Venzke et al. 2000; Lau and Nath 2004) via an atmospheric teleconnection. Modeling studies suggest that this anomalous pattern of SST counteracts and overwhelms a direct atmospheric forcing of ENSO on East African rainfall (Goddard and Graham 1999; Latif et al. 1999). Hence the basinwide SST anomaly pattern is considered important in the seasonal prediction of rainfall anomalies over East Africa. Recent modeling studies also suggest that this SST anomaly pattern may modulate the Pacific–North American (PNA) pattern forced by ENSO (Annamalai et al. 2005).

The Indian Ocean does not simply warm up in unison during ENSO (e.g., Nigam and Shen 1993). Rather, around boreal fall, prior to the ENSO winter peak, the far-eastern south Indian Ocean is typically cold (warm) during El Niño (La Niña). Modeling studies (e.g., Shinoda et al. 2004) suggest that these rather weak SST anomalies in the eastern equatorial Indian Ocean are also forced by surface heat fluxes associated with ENSO. This is accompanied by off-equatorial wind stress curl anomalies that force Rossby waves in the south-central Indian Ocean. The Rossby wave takes a few months to reach a shallow thermocline dome in the southwestern Indian Ocean where they manifest as SST anomalies augmenting the evolving basinwide pattern set in motion by the ENSO-forced heat fluxes (Xie et al. 2002). The off-equatorial Rossby wave requires

separate treatment since it involves ocean dynamics and hence will be examined further in section 3b.

Figure 3b summarizes the results from a lagged correlation analysis between the Niño-3 SST anomalies and a basin-averaged ( $20^{\circ}\text{S}$ – $20^{\circ}\text{N}$ ,  $40^{\circ}$ – $100^{\circ}\text{E}$ ) index of the Indian Ocean SST anomaly. In the observational–reanalysis datasets, the basinwide warming lags the Niño-3 peak by 4–6 months. In the coupled climate simulations a wide range of behavior is noted in both the maximum correlation of SST as well as its lag with Niño-3. About 4 of the 17 models show correlations weaker than 0.25 between the time series. One of the models, M14, is even negatively correlated, possibly because of a weak ENSO event in the Pacific. With respect to the time lag between the series, most simulations simulate a basinwide warming that peaks one to two seasons following the Niño-3 peak. However, in M2, M13, M7, and M8 the basinwide pattern peaks 8 months to 1 year following ENSO. The spatial signal of the basinwide pattern is further compared in Fig. 4 where the correlation map of Indian Ocean SST anomaly with Niño-3 is shown at the lags displayed in Fig. 3b. In this and the rest of the figures we do not map the simulations by M16 and M17, the two models with weakest Niño-3 standard deviation. M16 and M17 are also quite low resolution models and suffer from a deep and diffuse thermocline structure in the tropical Indian Ocean. Further, we map only one observational dataset from now on. Wherever appropriate, we have described the simulation of the omitted simulation–observation in words.

This, along with Fig. 1, suggest that models with reasonably strong ENSO variability are largely successful in simulating this delayed response in the Indian Ocean. Models M5, M8, and M12 are the exception: although having reasonable ENSO amplitude, they are unsuccessful in simulating the basinwide response of the Indian Ocean. Interestingly, the seasonality of ENSO in all three models is off by two seasons compared to observations (Fig. 3, left). M14, on the other hand, shows cool (warm) Indian Ocean SST anomalies in the central and eastern Indian Ocean in concert with El Niño (La Niña).

### c. ENSO teleconnection through oceanic processes

While the basinwide pattern manifests the thermodynamic response of the ocean mixed layer to ENSO, the other two patterns to be described below are due to ocean dynamics. To set the stage for the discussion of the dynamic response of the ocean, we shall first describe the mean setting of the ocean thermocline in relation to the wind field.

A unique aspect of the Indian Ocean is the presence

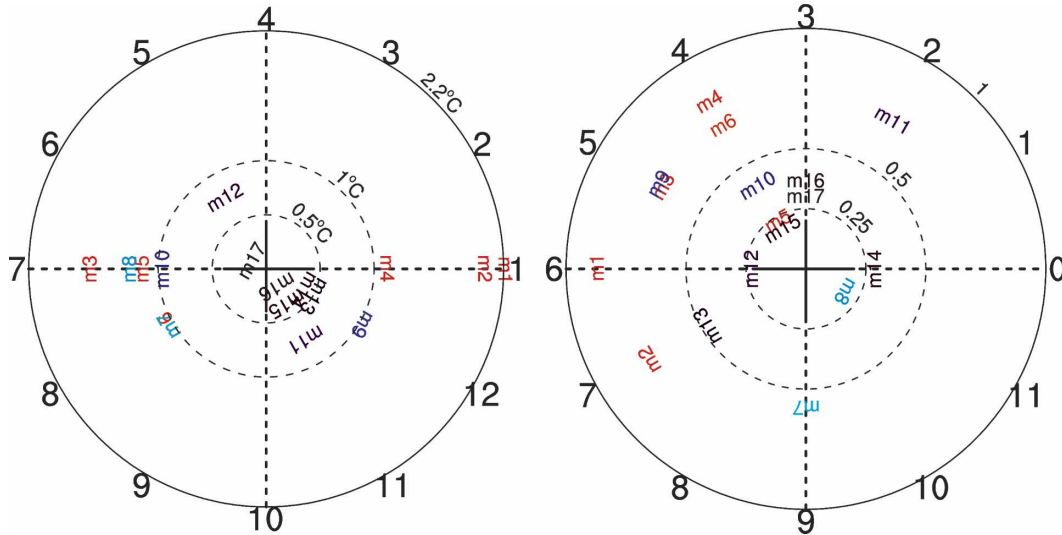


FIG. 3. (left) The month in which the standard deviation of Niño-3 peaks and its peak value. Numbers 1 to 12 on the outer circle indicate calendar months from January to December. In this polar plot, the magnitude of the Niño-3 standard deviation determines the distance of a model/observation from the center while the month of peak amplitude determines the angle (positive counterclockwise) that it makes with the  $x$  axis. (right) Maximum correlation between Niño-3 with basin-averaged ( $20^{\circ}\text{S}$ – $20^{\circ}\text{N}$ ,  $40^{\circ}$ – $100^{\circ}\text{E}$ ) Indian Ocean SST anomaly and the lag at which this maximum occurs. Numbers 0–11 on the outer circle indicate lags. The value of the correlation coefficient determines the radial distance while the lag determines the radial angle. Model labels are colored in rainbow colors from red to violet in descending order of Niño-3 index variance.

of equatorial westerlies in the central and eastern basin in the annual mean. Because of this, the thermocline slopes to the east, quite the opposite of the setting in the equatorial Pacific and Atlantic Oceans. The relatively deep equatorial thermocline is disrupted in three distinct regions of the Indian Ocean by wind-induced upwelling. The first of these occurs off the coast of Somalia where the strongest upwelling in the Indian Ocean takes place in the boreal summer season, driven by energetic monsoon winds. A second upwelling zone occurs off the coast of Java where the alongshore winds are southeasterly, favorable for coastal upwelling during late spring to early fall. Due to the strong annual cycle in the alongshore winds, this upwelling region occurs only during one-half of the year. We shall discuss this upwelling zone, which plays an important role in the dynamics of the IOD, in section 4.

The other region, located over the southwest Indian Ocean, is rather unique due to open ocean upwelling induced by the upwelling wind curl, which is in turn a consequence of the easterly trades recurving to become westerlies just south of the equator. A permanent feature throughout the annual cycle, this thermocline dome plays an important role in SST variability in the south Indian Ocean in response to ENSO (Xie et al. 2002). Recent studies (Saji et al. 2005b, manuscript submitted to *J. Climate*) have shown that the thermocline

dome plays an important role in regulating boreal winter air–sea interactions at intraseasonal time scales.

Figure 5 shows the annual mean distribution of thermocline depth (represented by the depth of the  $20^{\circ}\text{C}$  isotherm,  $D_{20}$  hereafter) over the tropical Indian Ocean. It is rather encouraging that the amplitude and location of the thermocline dome is reasonably well captured in many of the higher-resolution models. The two low-resolution models, M16 and M17 (not shown), have a too deep thermocline and conspicuously lack a dome structure in the south Indian Ocean. Among the higher-resolution models, M9 has the dome situated at the right location, but is too deep relative to the SODA reanalysis. On the other hand, in M15 the dome is erroneously simulated in the southeastern Indian Ocean. The consequences of these discrepancies in thermocline structure will be apparent in the following analysis.

Klein et al. (1999) note that surface heat flux explains the Indian Ocean SST response to ENSO except over the southwestern basin, a result confirmed by simulations with coupled atmospheric GCM–ocean mixed layer models (Alexander et al. 2002). Instead, a significant part of SST variability over the southwest Indian Ocean is due to ocean Rossby wave forces in midbasin by ENSO-induced wind changes (Xie et al. 2002). Near the equator, the IOD also plays a role in forcing Rossby waves in the ocean (Rao and Behera 2005).

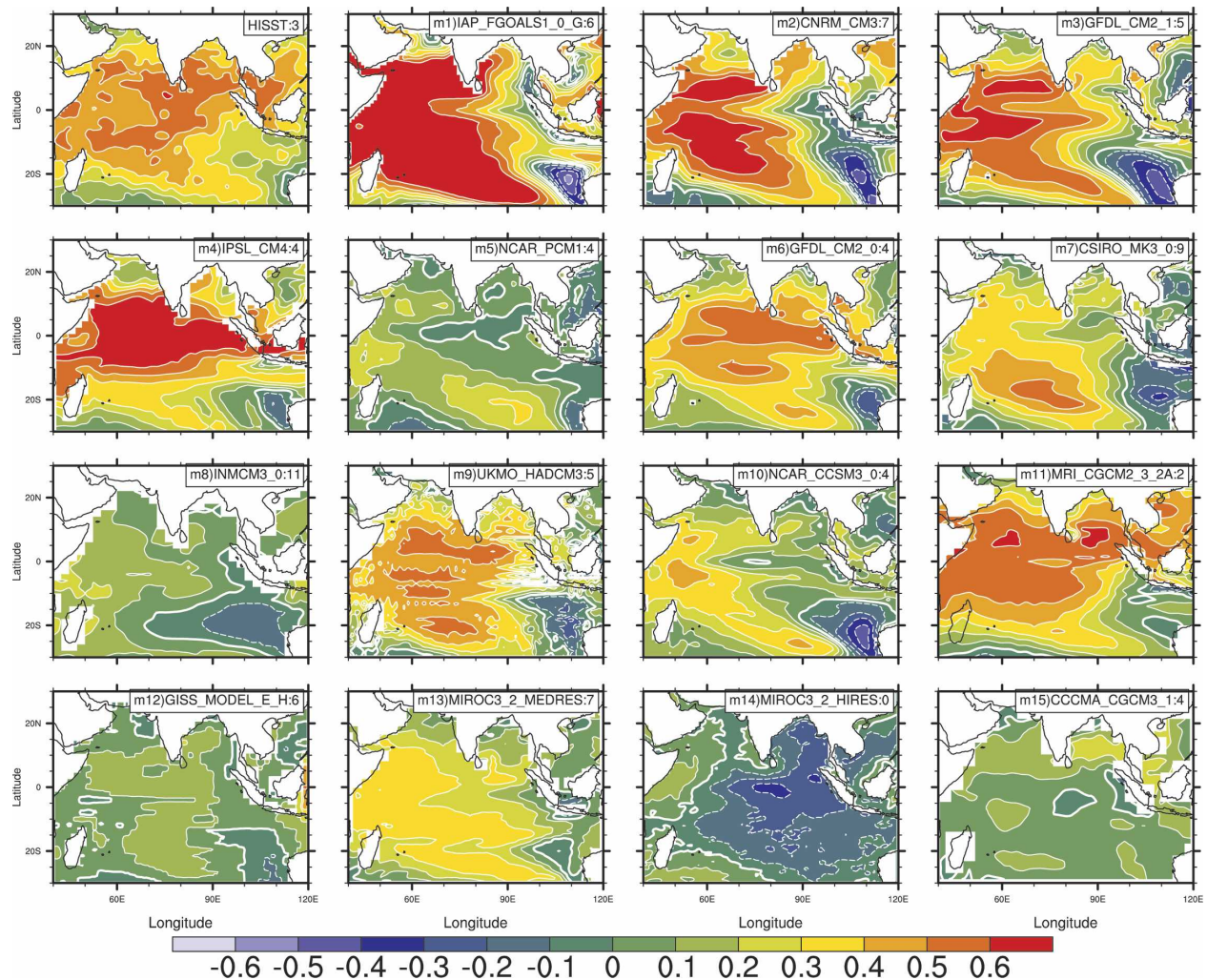


FIG. 4. Spatial structure of the correlation between Niño-3 and Indian Ocean SST anomalies at the lag of maximal correlation. The lag of maximum correlation is indicated after the model label separated from it by a colon; the thick white line depicts the zero contour.

This oceanic Rossby wave effect is summarized in Fig. 6. In SODA, high thermocline depth variance is found in the south Indian Ocean, and the thermocline feedback is strong in the western basin over the thermocline dome. In the south Indian Ocean, oceanic Rossby waves are excited in the central basin as the Pacific ENSO reaches its peak. As these waves travel westward, a copropagation of SST anomalies is clearly visible in the SODA reanalysis, indicative of the thermocline feedback on SST due to the shallow thermocline depth.

All of the models appear to capture the enhanced positive correlation between thermocline depth and SST over the dome of the southwestern tropical Indian Ocean, indicative of a thermocline feedback on SST there. Models with reasonably large ENSO variability,

except for M5 and M8, generally produce quite large thermocline depth variability due to oceanic Rossby waves in the southwestern Indian Ocean: in M5 and M8, Niño-3 peaks in July. In the rest of the models, marked Rossby waves are excited by an ENSO-induced teleconnection in surface wind and propagate westward across the basin (Fig. 6). While the SST copropagation is not as clear as in the SODA observations, these Rossby waves help prolong SST correlation along their path toward the west two seasons after the ENSO dissipates in the Pacific. This enhanced SST correlation due to oceanic Rossby wave propagation becomes more pronounced if the zonal means are removed (not shown). In those models with a weak ENSO (M12–M17), either Rossby waves or their SST effects are weak.

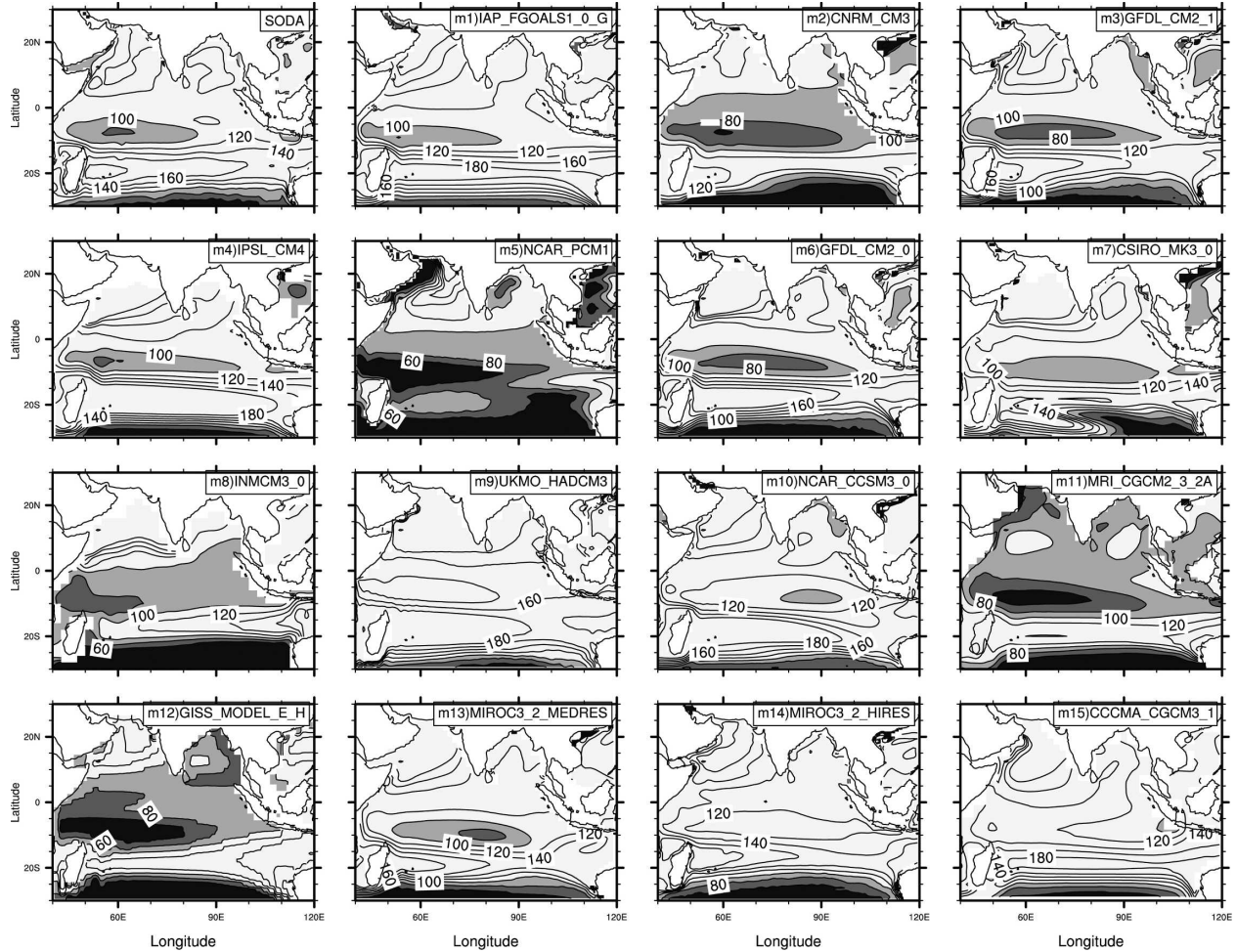


FIG. 5. Annual mean distribution of depth of the 20°C ( $D_{20}$ ) isotherm (m) in SODA and climate simulations. Contours are from 60 to 180 m at intervals of 20 m (shading  $\leq 100$  m).

A second ENSO teleconnection with the Indian Ocean SST that involves ocean dynamics is associated with the propagation of sea level and thermocline anomalies into the eastern Indian Ocean from the equatorial western Pacific. During an El Niño, for instance, the sea level is anomalously low in the western equatorial Pacific resulting from the propagation of upwelling equatorial Rossby waves into this region from the central Pacific. Since the western boundary of the Pacific is full of gaps, part of the wave energy penetrates into the Indian Ocean from the point northwest of Iryan Jaya, where the Australasian landmass meets the Pacific equator (Clarke and Liu 1994; Meyers 1996; Verschell et al. 1995; Potemra 2001). After crossing the equator, it travels as a coastally trapped wave down the western coast of Australia, radiating Rossby waves at a critical latitude (Clarke and Liu 1994) around 20°S. The presence of the dynamic ocean variability is clearly ex-

pressed in SSTs (Meyers 1996; Saji and Yamagata 2003b).

The presence of the throughflow wave signal can be depicted in observed SST by correlating equatorial Pacific zonal winds with SST, after accounting for the effect of equatorial zonal winds in the Indian Ocean (Meyers 1996; Saji and Yamagata 2003b; Wijffels and Meyers 2004), using partial correlation/regression techniques. The partial correlation of SST on equatorial Pacific winds is shown in Fig. 7 for the observed and simulated SSTs. The signal of the Rossby-coastal Kelvin wave dynamics in the genesis of eastern Indian Ocean SST anomalies is clearly evident in HISST, as well as in OISST and SODA (not shown).

Model simulations of this important pattern are expected to be closely tied to the representation of topography and coastline curvature in numerical models (Li and Clarke 2004; Cai et al. 2005) as well as the vertical

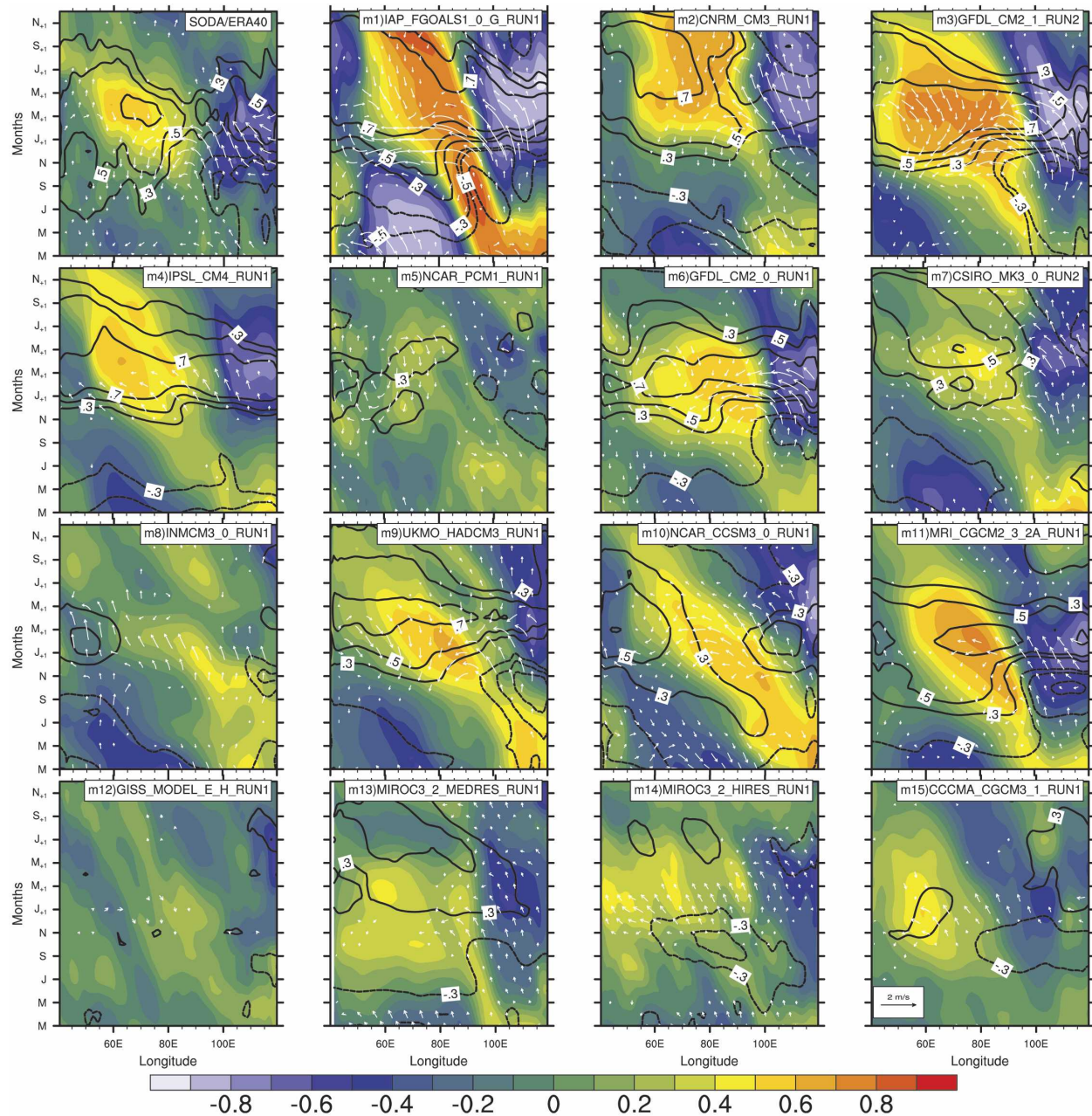


FIG. 6. Lagged correlation of OND Niño-3 with SST (shaded) and  $D_{20}$  (line contour). Line contours are at  $\pm 0.3, 0.5, 0.7,$  and  $0.9$ . Vectors depict the lagged regression of Niño-3 on surface wind velocity. SST,  $D_{20}$ , and wind anomalies were averaged between  $12^{\circ}$  and  $8^{\circ}$ S.

density structure in the ocean. Models that have coarse resolution and unrealistically wide gaps in the Indonesian throughflow region (ITF) simulate a turning latitude for waves that are much closer to the equator than is observed (M9, M11). However, barring M2 and M10, none of the models, including the higher-resolution ones, are able to capture this feature.

The distorted oceanic teleconnection is likely to have

an impact on simulations of IOD variability. In exploring the unrealistic IOD in the Commonwealth Scientific and Industrial Research Organisation (CSIRO) Mark 3 model, Cai et al. (2005) found that the unrealistic representation of the model's Java-Timor geometry resulted in an artificial pathway for Pacific upwelling Rossby waves to reach the model Java coast, triggering an IOD event about 6–9 months after the ENSO peak.

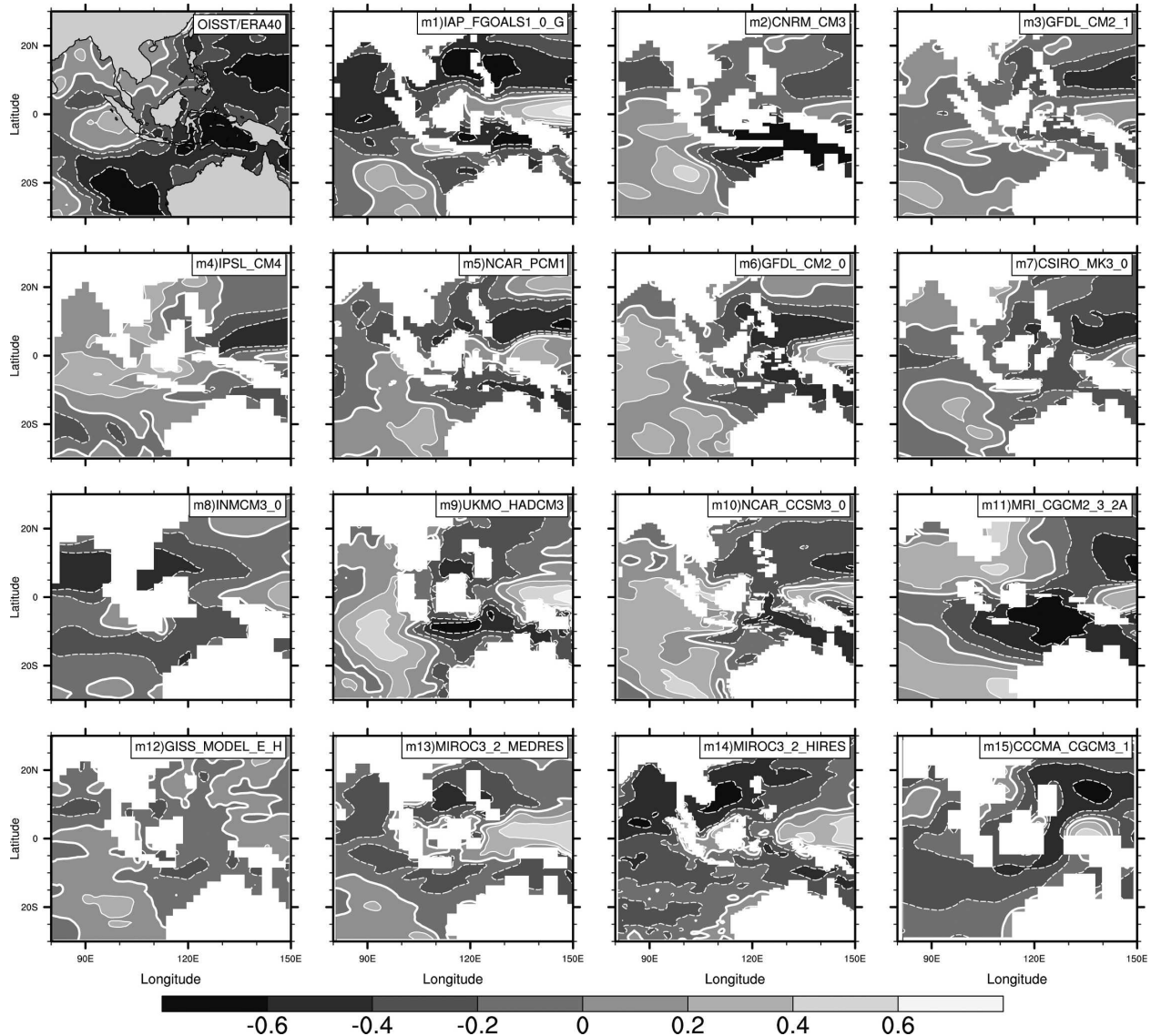


FIG. 7. The partial correlation of Indian Ocean SST with equatorial Pacific zonal winds after accounting for the effect of equatorial Indian Ocean zonal winds on the SST. Thick white line depicts the zero contour.

Analysis of observations, on the other hand, shows that there is no pathway for Pacific Rossby waves to reach the Java coast (Clarke and Liu 1994; Wijffels and Meyers 2004). The Cai et al. (2005) results highlight the importance of proper topographic and geographic representation of the Indonesian region in modeling variability of the Indian Ocean.

The oceanic teleconnection of ENSO through the ITF is also important to the regional climate and environmental variability of the Maritime Continent, as discussed below, and hence its poor representation in models is discouraging. SST anomalies associated with the throughflow wave signal are significantly associated with rainfall variability over Australia (Meyers 1996).

Drought bad enough to have a damaging economic impact occurs when the SST in the Indonesian region is anomalously cool (Nicholls 1989; Drosowsky 1993). The dynamic signal of the ITF wave travels quite far along the Australian coast and can be detected in altimetric sea level data as far as the south coast of Australia to the southern tip of Tasmania (Wijffels and Meyers 2004). A consequence of the lower sea level is a decrease in the baroclinic pressure gradient between northwestern Australia and Java. At interannual frequencies, by geostrophy, this corresponds to a weakening of the Indonesian throughflow during El Niño (Meyers 1996). The anomalous sea level changes further modulate shelf currents and affect the March–

September eastward transport of Australian salmon larvae from western Australia, enhancing recruitment in the eastern nursery grounds when the March–September sea level is anomalously high (during La Niña) and decreasing it when it is low (Li and Clarke 2004).

#### 4. The Indian Ocean dipole

The IOD is a basin-scale pattern of SST and wind anomalies occurring on interannual time scales in the equatorial Indian Ocean (Saji et al. 1999; Webster et al. 1999; Murtugudde et al. 2000). When the SST is anomalously cool in the east and warm in the west during the peak phase of a positive IOD event, the equatorial winds reverse their direction from westerlies to easterlies. The wind is coupled to SST in the sense that it blows from the cooler toward the warmer waters. The coupled anomalies of SST, wind, and rainfall have a major impact on seasonal climatic conditions in nations around the Indian Ocean, sometimes even stronger than the impact of ENSO (Saji and Yamagata 2003a). Many (but not all) positive IOD events occur during the same year as El Niño, and the same can be said about negative IOD events and La Niña (Saji and Yamagata 2003b).

Observational analysis suggests that IOD variability is not merely a forced response to ENSO. For instance some strong IOD events take place during weak or non-ENSO years (Saji et al. 1999; Shinoda et al. 2004; Yamagata et al. 2004), suggesting that Bjerknes feedback between thermocline and zonal wind can generate an unstable growth of an initial perturbation. Hence, if conditions for unstable growth are met, IOD variability can be triggered by phenomena other than ENSO. Lau and Nath (2004) examined IOD events in a 900-yr integration of the Geophysical Fluid Dynamics Laboratory (GFDL) CGCM. They found that perturbations associated with the Southern Annular Mode could provide a trigger for the IOD events that occurred in the absence of ENSO. Fischer et al. (2005) took a further step, conducting twin CGCM experiments to investigate the independent behavior of the IOD from ENSO. A control experiment was compared to a run in which ENSO behavior was artificially suppressed. The latter (no ENSO) run also produced realistic IOD variability, suggesting that the IOD is associated with an unstable Bjerknes feedback in the equatorial Indian Ocean. In their no-ENSO run, the occurrence of IOD events was about half as often as that in the control run. They found that meridional circulation anomalies during the onset of the monsoon were an important trigger for IOD generation. Behera et al. (2005) also conducted a

twin experiment with the Scale Interaction Experiment (SINTEX) CGCM and arrived at a similar conclusion as Fischer et al. regarding the generation of the IOD by unstable air–sea interactions. Here we point out that, while IOD variability is considered to arise from unstable Bjerknes feedback, this does not imply the existence of a self-sustained oscillation. Rather, the IOD is likely a damped oscillator that requires a trigger to excite.

##### a. Mean state

We begin our IOD analysis by examining the mean state along the equator (Fig. 8) since it is critical to the equatorial mode of the Bjerknes feedback (Neelin et al. 1998; Xie et al. 1999). Almost all of the models (with M2 as the exception) simulate warm SSTs that are nearly uniform east of 60°E within a range of 27.5°–29.5°C. All models capture the SST cooling and suppressed convection in the west off Africa. The success in simulating the eastward increase in equatorial rainfall is much more varied. With a few exceptions, mean winds are weak on the equator, generally less than 2 m s<sup>-1</sup>. As a result, the thermocline is quite flat along the equator, much as in observations. With the exception of M16 and M17 (not shown), the zonal-mean thermocline depth ranges from 80 to 160 m, as opposed to the observed value of 110 m. Overall, the models show high skill in simulating the zonal distributions of SST, thermocline depth, and precipitation along the equator in contrast to their poor skill in the equatorial Atlantic (Davey et al. 2002), an ocean of a similar zonal width that is also subject to strong land influences (e.g., Okumura and Xie 2004).

##### b. Spatial patterns

Several indices have been proposed to identify the IOD pattern from observations. These include the dipole mode index (DMI), an index of the large-scale zonal SST gradient between the western and eastern Indian Ocean (Saji et al. 1999), time series of SST anomalies in the eastern Indian Ocean [Sumatra cooling index; Xie et al. (2002)], and the leading principal component of ocean temperature anomalies in the equatorial depth plane (Shinoda et al. 2004). Since SST variability in the Indian Ocean is composed of multiple factors (Saji and Yamagata 2003b), isolating the different patterns from each other is not always easy. The DMI was designed to separate the IOD pattern from the basinwide warming pattern directly forced by ENSO by subtracting the western Indian Ocean SST anomalies from the eastern Indian Ocean anomalies. However, the DMI implicitly assumes a particular di-

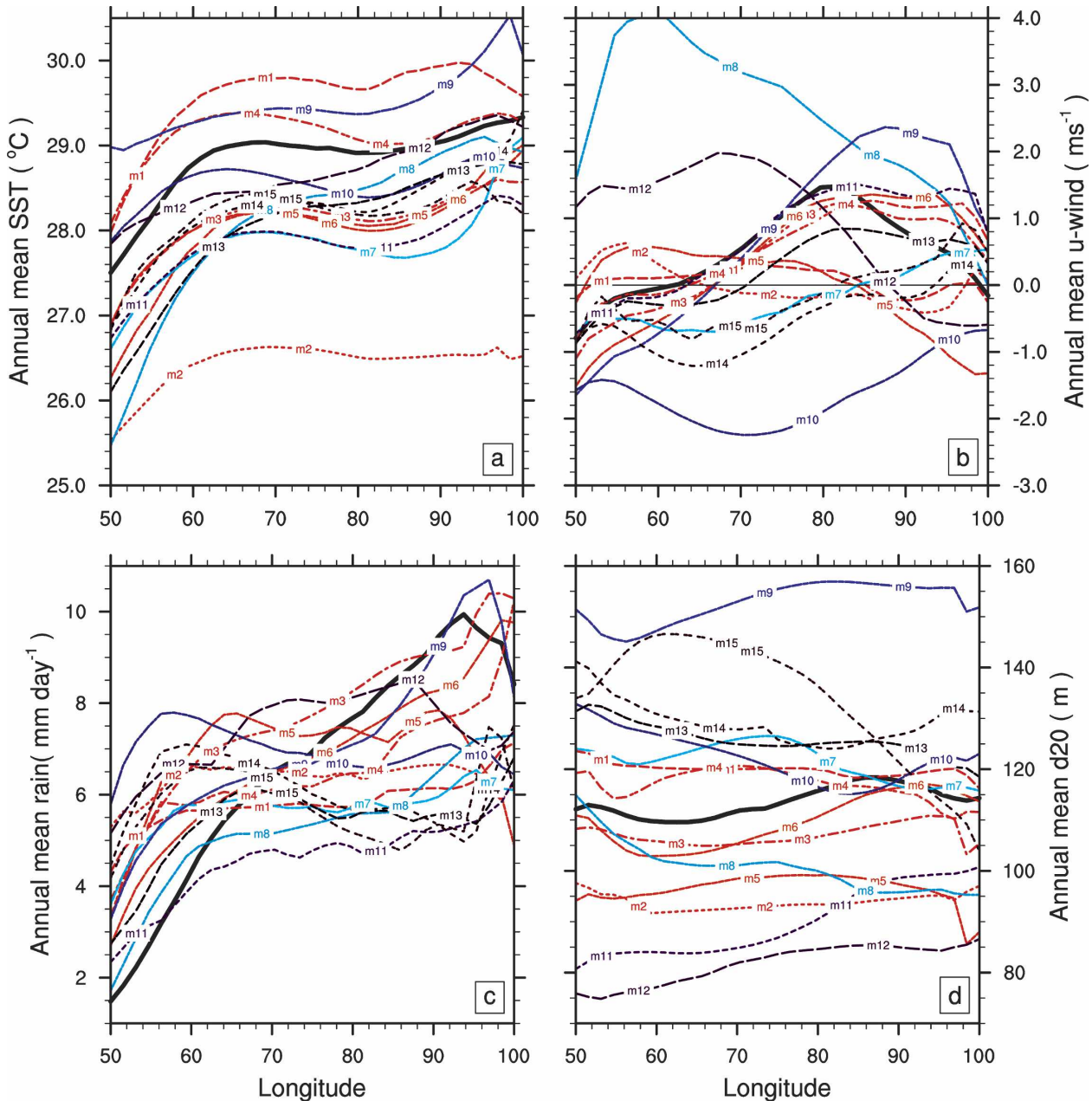


FIG. 8. Annual-mean equatorial climatologies for (a) SST, (b) zonal wind, (c) rain, and (d)  $D_{20}$  in climate simulations and observations (black curve). For the observational curves, SODA is used for SST and  $D_{20}$ , CMAP for rain, and ERA40 for zonal winds. Model curves are colored in rainbow colors from red to violet in descending order of Niño-3 index variance.

polar structure of the SST anomaly that is not always realized in model simulations of the IOD. The Sumatra cooling index focuses on the more robust and stronger part of SST variability during IOD events in the eastern Indian Ocean. However, eastern Indian Ocean SST anomalies are also strongly influenced by the basinwide pattern. Therefore, the Sumatra cooling index may sometimes contain influences of both patterns. The index designed by Shinoda et al. (2004) realizes the im-

portance of ocean dynamics in the generation of SST anomalies during the IOD. Since the basinwide SST warming does not involve ocean dynamics, this index can effectively isolate the IOD pattern. This index is strongly correlated to the DMI in observations. An advantage of the index is that it does not impose the dipolar structure in SST as required by the DMI.

In this study we will use a modified form of the Shinoda et al. index. Instead of using the first principal

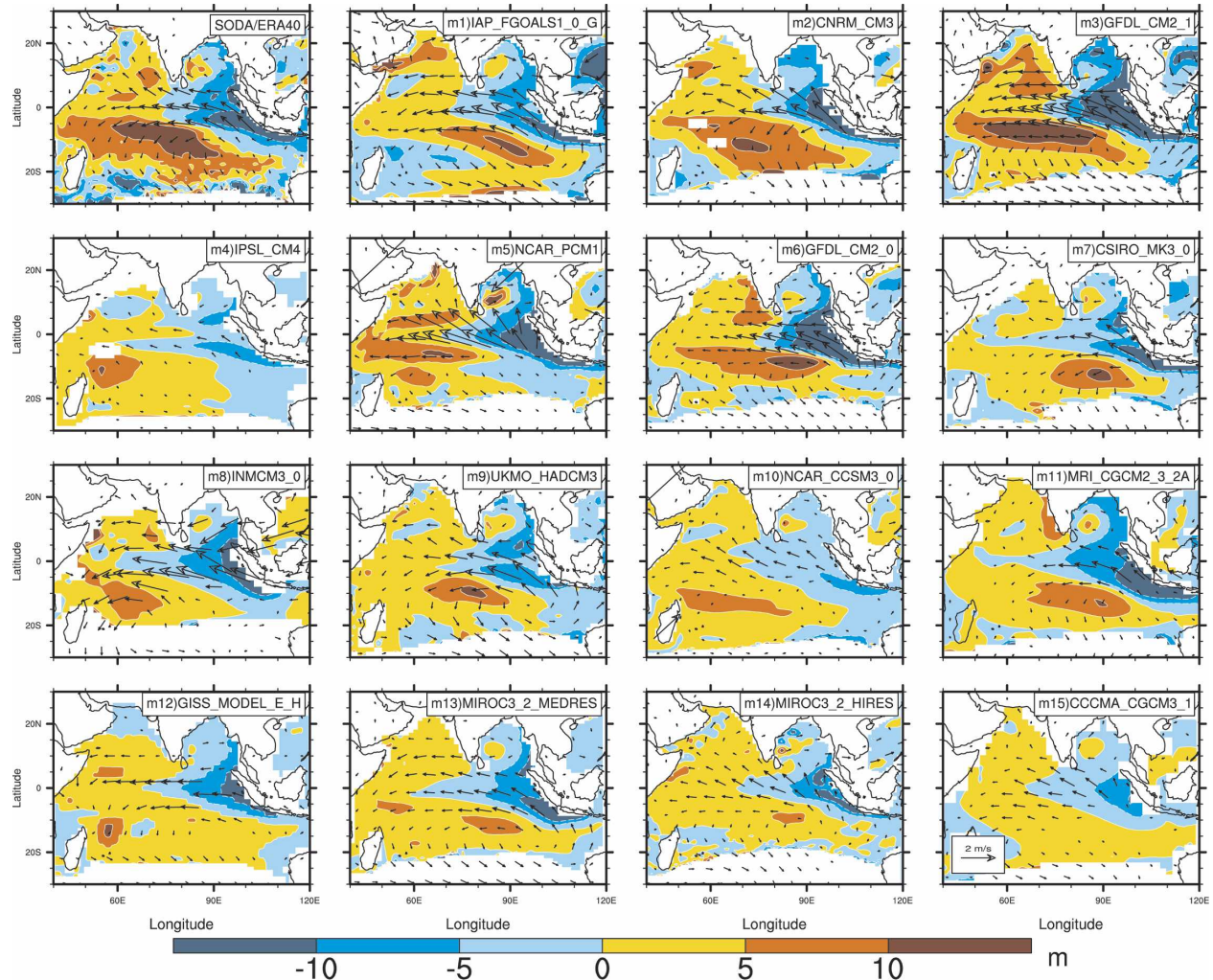


FIG. 9. Linear regression of  $D_{20}$  (shaded, m) and surface winds (vectors,  $\text{m s}^{-1}$ ) on the PC1 of  $D_{20}$  for observations and climate simulations.

component time series (hereafter PC1) of equatorial depth temperature sections, we will use the PC1 of  $D_{20}$  between  $20^{\circ}\text{S}$  and  $20^{\circ}\text{N}$ . Since the pattern of the IOD predominates tropical Indian Ocean subsurface temperature anomalies (Rao et al. 2002) in observations, the two are, in fact, equivalent.

Figure 9 shows the linear regression maps of  $D_{20}$  upon the PC1 time series of  $D_{20}$  during September–November (SON). The vectors represent the regression of surface winds on the PC1 time series. The SST pattern associated with the PC1 time series is shown in Fig. 10. For the observations, this yields the well-known IOD pattern at its mature phase. It shows easterly wind anomalies well trapped at the equator around the central Indian Ocean. This is associated with a shoaling of the thermocline to its east and a deepening to its west. The shape of the thermocline anomalies shows the ex-

pected features arising from equatorial and coastal Kelvin waves and radiating/wind-forced Rossby waves. The cooling of SST anomalies is asymmetric about the equator as in Saji et al. (1999) because of the difference in thermocline–SST coupling south and north of the equator in the eastern Indian Ocean (Rao and Behera 2005).

It is encouraging that most of the models analyzed here develop features similar to observations, except for M16 and M17 (not shown). M16 and M17 are too coarse to efficiently resolve equatorial Kelvin wave processes. Hence their lack of IOD activity is not surprising.

Figure 10 shows SST and rainfall anomalies associated with the IOD in the different models. All of the models shown in the figure simulate the out of phase relation between rainfall anomalies in the eastern and

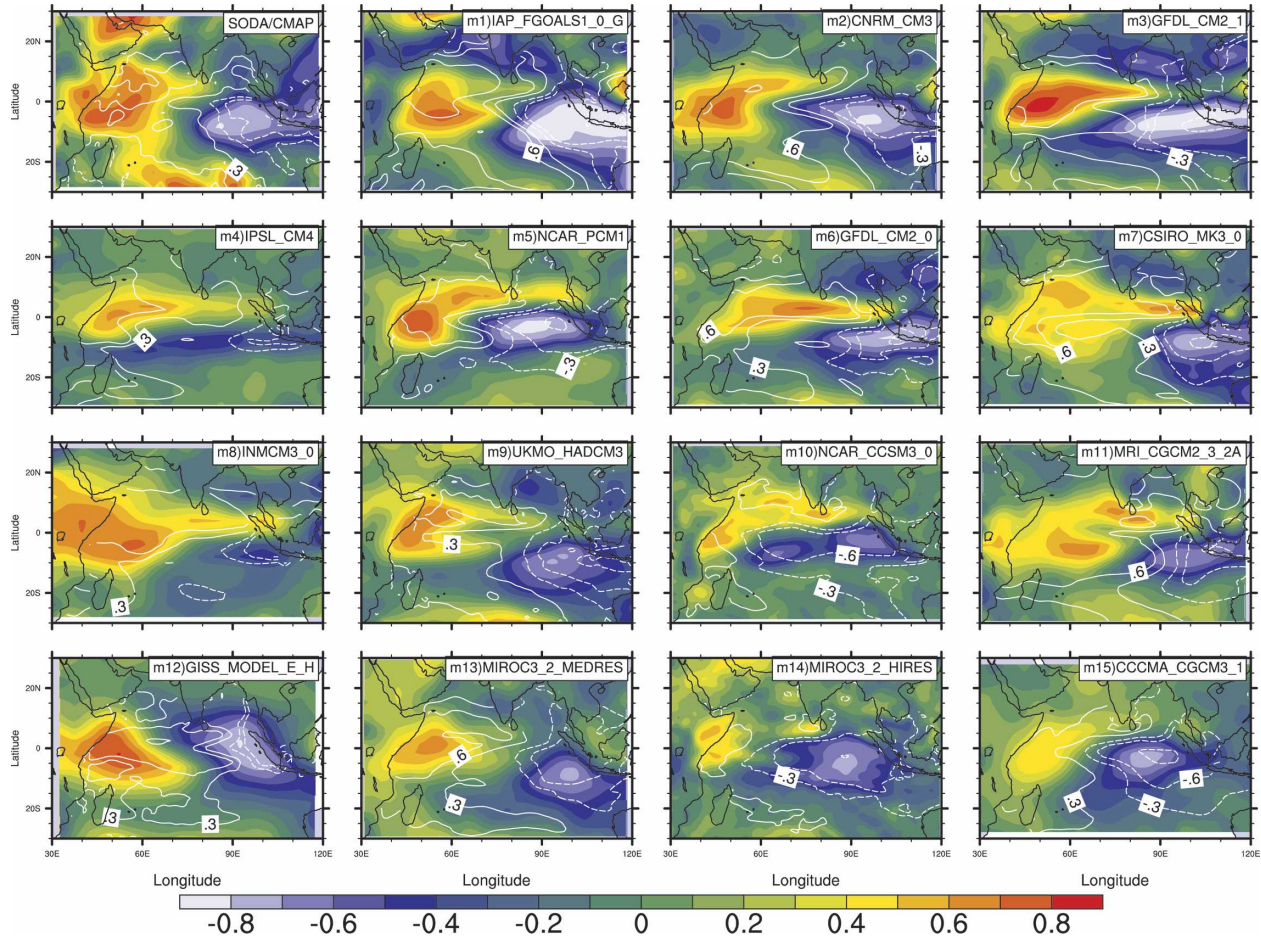


FIG. 10. Correlation of SON rainfall (shaded) and SST anomalies (contour) with the PC1 of SON  $D_{20}$  in observations and climate simulations. Contours are shown at  $\pm 0.3$ , 0.6, and 0.9.

western equatorial Indian Ocean typical of the IOD, except for M14 in which rainfall anomalies are somewhat weaker over the west. This is due to the anomalous cold tongue in the east extending too far westward in this model, almost reaching the African coast.

### c. Seasonality, feedback, and forcing

IOD evolution shows strong seasonality in the observations (Saji et al. 1999) because upwelling-favorable winds are observed off the west coast of Sumatra only during June–October (Xie et al. 2002). To assess this aspect in the models, we show in Fig. 11 the standard deviation of DMI in the coupled simulations and OISST (thick black line) as a function of calendar month. We note that the standard deviation of DMI in SODA is quite similar to that in OISST, but the DMI variability in HISST is somewhat weaker, possibly an artifact of the reconstruction methodology used to de-

rive that product since the real observations [Comprehensive Ocean–Atmosphere Data Set (COADS)] has a DMI variance similar to that of SODA and OISST (Saji and Yamagata 2003b). All models reasonably capture the observed seasonal evolution of the DMI variability, showing enhanced variability in the second half of the year. The peak month of DMI variance and its amplitude, however, shows considerable spread among different model simulations with most showing a peak in SON, as noted. In a few models, however, the IOD persists after SON.

Figure 12 shows scatterplots between PC1 of  $D_{20}$ , zonal SST gradient (DMI), equatorial zonal winds, and ENSO (Niño-3) for climate models during boreal fall. There is a strong and self-consistent relation between depth of the thermocline, SST, zonal equatorial winds, and rainfall, indicative of the Bjerknes feedback among these variables (Xie et al. 2002). As in the observations (Saji and Yamagata 2003b; Shinoda et al. 2004), the

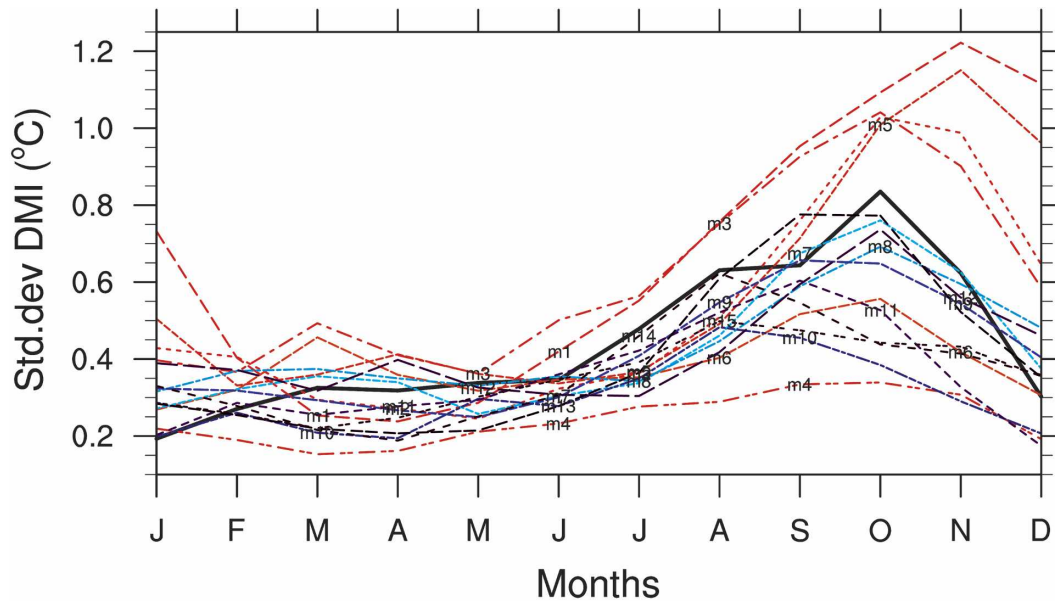


FIG. 11. Standard deviation of the zonal SST gradient as a function of season is shown for OISST (thick black line) and climate simulations. Model curves are colored in rainbow colors from red to violet in descending order of Niño-3 index variance.

relation between the IOD and Niño-3 in the models is weaker, suggesting that ENSO is one but not the only trigger for the IOD.

Finally, we investigate the possible controls of the IOD in the climate simulations. Modeling studies (e.g., Iizuka et al. 2000; Gualdi et al. 2003; Spencer et al. 2005; Fischer et al. 2005) have suggested that the intensity of climatological coastal upwelling off the Java coast is important in initiating the unstable Bjerknes feedback during the IOD. To examine this possibility, we plot in Fig. 13a the relation between  $D_{20}$  off Java (area average between  $15^{\circ}$  and  $5^{\circ}$ S,  $105^{\circ}$  and  $115^{\circ}$ E) during June–November (JJASON, the upwelling season) and the interannual standard deviation of DMI (PC1 of  $D_{20}$ ) during SON. To isolate regions associated with upwelling, we only consider grids that have values of 100 m or less in the calculation of the area-averaged  $D_{20}$ . If we exclude outliers M3 and M15, there is a weak tendency for larger DMI variance with a shallower thermocline off Java but the scatter is quite large. The large diversity in the relation may be due to the diversity in other aspects of ocean–atmosphere coupling among the different models. The strong preference of the model IOD for August–November (see Fig. 11) suggests that coastal upwelling is important for developing a zonal mode in the equatorial Indian Ocean.

To examine the possibility that the IOD variability in the simulations is merely a slave to ENSO, we examine the relationship between the strength of Niño-3 during boreal fall to the correlation between the IOD and

ENSO during the same season (Fig. 13b). For this relation to exist we expect stronger correlations between DMI and Niño-3 in models with strong Niño-3 variations. Examination of Fig. 13b does not suggest a significant relation between the two quantities, even if we remove the two apparent outliers M1 and M2.

Thus, the climate simulations suggest that the IOD is not a mere slave to ENSO. Previous modeling studies (Meehl et al. 2003; Fischer et al. 2005; Wajsowicz 2005; Spencer et al. 2005) suggest that the triggering effect of ENSO on the IOD is through Walker circulation anomalies that introduce surface wind anomalies and consequently thermocline depth anomalies in the equatorial eastern Indian Ocean. On the other hand, the IOD may also be affected by other phenomena that introduce perturbations to the Java upwelling zone. Wind anomalies associated with interannual monsoon variations (Wang et al. 2003; Fischer et al. 2005), intraseasonal variability (Rao and Yamagata 2004), and the Southern Annular Mode (Lau and Nath 2004) are some possible triggers for the IOD. It may then be argued that the efficacy of these triggers would depend on the strength of the thermocline–SST feedback in the Java upwelling zone, which in turn is a function of the mean depth of the thermocline in that region. If this is true, we expect models that have a deep thermocline near Java to be predominantly affected by the ENSO, but those with stronger thermocline–SST coupling to be also affected by triggers other than ENSO. To examine the control of thermocline–SST coupling off Java on

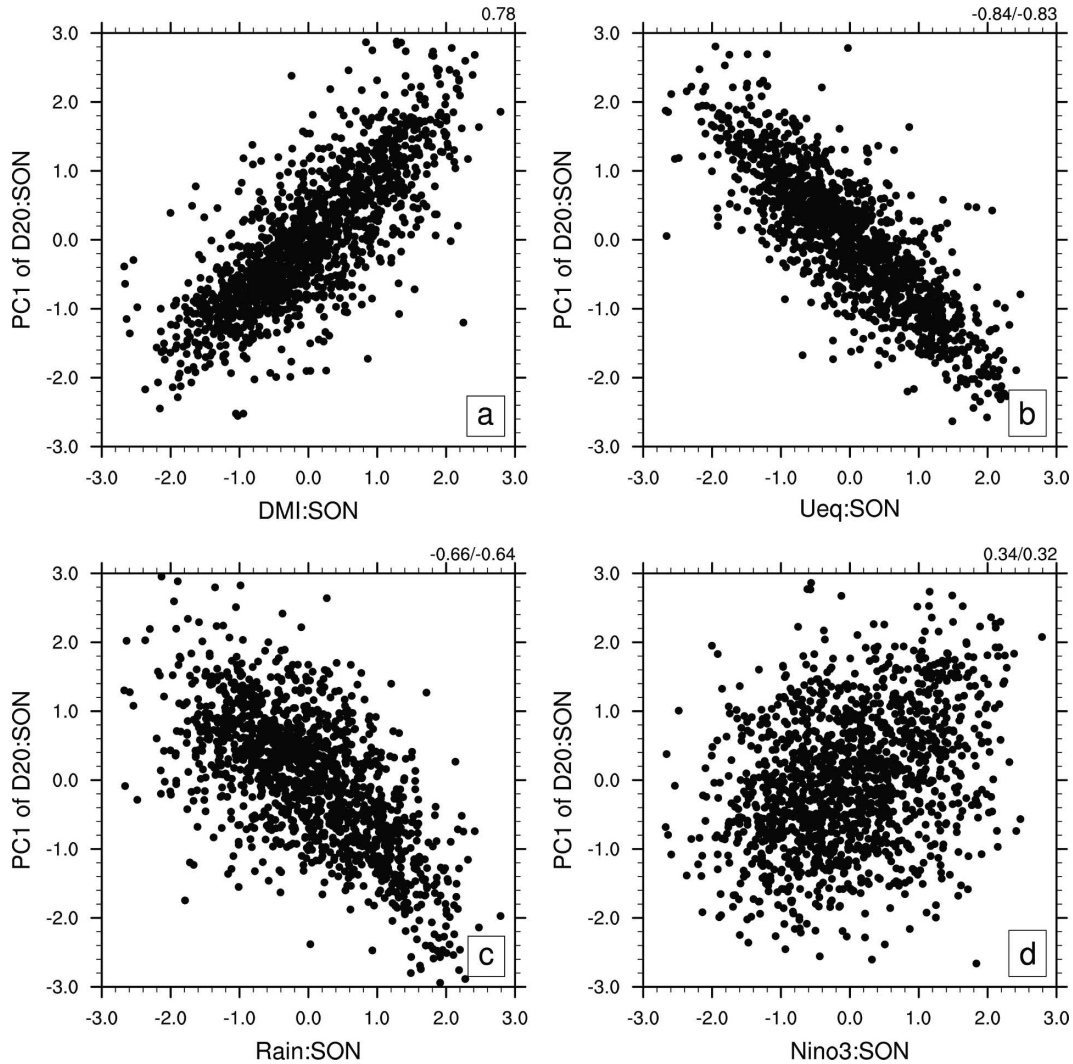


FIG. 12. Relation of PC1 of  $D_{20}$  during SON with the (a) equatorial zonal SST gradient, (b) equatorial zonal winds, (c) rain over south equatorial Indian Ocean, and (d) Niño-3, shown for SON in all models. The pooled correlation for all the models between PC1 and each variable is shown in the top-right side of each panel, and that between DMI and each variable is shown to its right, with both separated by a forward slash.

the ENSO–IOD correlation, we plot in Fig. 13c the  $D_{20}$  off Java (averaged between  $105^{\circ}$  and  $115^{\circ}\text{E}$ ) against the DMI–Niño-3 correlation during SON. With M2 and M10 as exceptions we find that there is a tendency for shallower  $D_{20}$  models to have lower IOD–ENSO correlation and vice versa for deeper  $D_{20}$  models, in support of our hypothesis.

## 5. Summary

The multitude of SST variability mechanisms render CGCM simulations of Indian Ocean SST challenging. CGCMs must not only realistically simulate forcings such as monsoons and ENSO, but also their effects on

SST. Further, the interaction of the forced response with internal coupled modes like the IOD have to be properly represented. An accurate simulation of these for a wide spectrum of SST variability is important, as these patterns have significantly different climate impacts collectively and individually. This study has compared and evaluated simulations, using 17 coupled GCMs, of the major modes of SST variability on inter-annual time scales.

We first examined the different SST patterns associated with ENSO. The ENSO impacts Indian Ocean SST variability through thermodynamic atmospheric forcing as well as ocean dynamics. The thermodynamic forcing results in basinwide SST anomalies of the same

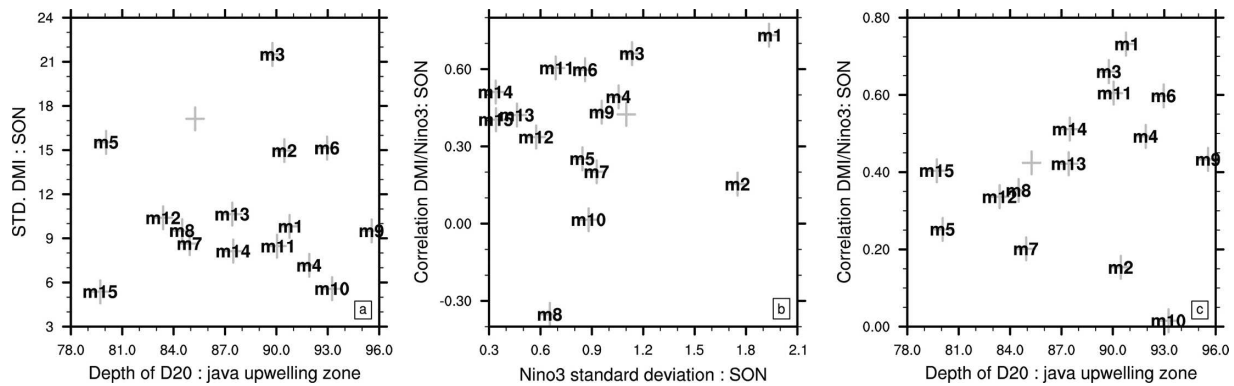


FIG. 13. Scatterplots between (a)  $D_{20}$  (m) in the Java upwelling zone during JJASON and standard deviation of DMI during SON, (b) standard deviation of Niño-3 ( $^{\circ}\text{C}$ ) and the correlation between DMI and Niño-3 during SON, and (c)  $D_{20}$  off Java (m) during JJASON and correlation between Niño-3 and DMI during SON.

sign over the tropical Indian Ocean, a few months following the peak of ENSO. Oceanic dynamics are important for two patterns of SST response to ENSO. The first is ocean–atmosphere coupled Rossby waves triggered by an ENSO-induced wind stress curl over the central Indian Ocean. Due to their slow propagation across the basin, the coupled Rossby waves prolong the influence of ENSO in the region by several months after the demise of an ENSO event. The second oceanic teleconnection of ENSO involves the propagation of equatorial oceanic waves from the western Pacific into the southeastern Indian Ocean through the Indonesian archipelago, affecting SSTs off the northwest Australian coast.

Our analysis reveals a serious problem in many climate models in simulating the ENSO teleconnections into the Indian Ocean. The problem is seen in all three of the ENSO-related SST patterns described above. Only 8 of the 17 CGCMs examined in this study simulated the basinwide SST anomalies following ENSO. A similar number of CGCMs captured the off-equatorial wind stress curl and thermocline variability associated with the coupled Rossby wave. On the other hand, virtually none of the models correctly simulated the SST anomalies off Australia associated with the through-flow wave propagation from the Pacific. It is beyond the scope of this paper to systematically explore the reasons for these deficiencies in simulating the Indian Ocean response to ENSO, but the amplitude of the simulated ENSO in the Pacific appears to be a factor. Models with a weak ENSO tend not to fare well in simulating the Indian Ocean response, presumably because of interference from other sources of variability. Another factor may be related to the simulation of mixed layer physics, including thin low salinity layers and barrier layers in the oceanic component of the CGCMs.

On the other hand, it is encouraging that a majority of the models succeeded in capturing IOD variability reasonably well. A major factor in simulating the IOD appears to be the mean thermocline depth in the equatorial regions during the latter half of the year. All models that simulated an IOD also simulated realistic mean thermocline depths over the eastern Indian Ocean, a key region for IOD variability. On the contrary, models that had a too deep thermocline failed to simulate any IOD variability. The simulated IOD in most of the models agrees reasonably with observations in spatial pattern and temporal evolution. In support for the importance of ocean–atmosphere coupling and positive feedback, the simulated IOD in the models features a strong coupling between rainfall, winds, thermocline, and SST anomalies. Models that simulate the IOD also simulate the observed out-of-phase relation between rainfall anomalies in the eastern and western Indian Ocean.

In summary, CGCMs are only partially successful in simulating the rich spectrum of SST variability in the Indian Ocean. At large, most models reproduce the SST variations that arise from local air–sea interaction (IOD), but many of them fail to adequately simulate the responses to ENSO. The implications of this deficiency are significant, both for the prediction of present as well as future climate. ENSO is an important forcing of Indian Ocean variability, accounting for a significant fraction of SST and rainfall variability in the Indian Ocean region. It is also one of the important triggers for the IOD. In a changing climate, ENSO may alter its characteristics (Timmermann et al. 1999) and hence its impact on Indian Ocean climate through altered teleconnection processes. Thus, it is of prime importance for CGCMs to simulate SST variability and its climate impacts realistically in both the Pacific and Indian Oceans, as these models are used to project climate

changes and their regional distributions. The possibility that Indian Ocean SST variations exert influences on ENSO and beyond, as suggested by recent studies (Saji and Yamagata 2003a,b; Giannini et al. 2003; Annamalai et al. 2005), adds more importance in their simulation in climate models.

*Acknowledgments.* We greatly appreciate the comments, suggestions, and criticism offered by the two anonymous reviewers, the editor Prof. Sumant Nigam, and Dr. Gary Meyers. We thank the Asia Pacific Data Research Center (APDRC), Ron Merrill, Sharon De Carlo, and in particular Jan Hafner for data and computational support. We acknowledge the international modeling groups for providing their data for analysis, the Program for Climate Model Diagnosis and Intercomparison (PCMDI) for collecting and archiving the model data, the JSC/CLIVAR Working Group on Coupled Modelling (WGCM) and their Coupled Model Intercomparison Project (CMIP) and Climate Simulation Panel for organizing the model data analysis activity, and the IPCC WG1 TSU for technical support. NCAR Command Language (NCL) was extensively used for computations and graphics. NCL is a free interpreted language designed specifically for scientific data processing and visualization (information online at <http://www.ncl.ucar.edu>). The IPCC Data Archive at Lawrence Livermore National Laboratory is supported by the Office of Science, U.S. Department of Energy. This work is supported by the Japan Agency for Marine–Earth Science and Technology and NASA.

#### REFERENCES

- Alexander, M. A., I. Bladé, M. Newman, J. R. Lazante, N.-C. Lau, and J. D. Scott, 2002: The atmospheric bridge: The influence of ENSO teleconnections on air–sea interaction over the global oceans. *J. Climate*, **15**, 2205–2231.
- Annamalai, H., S.-P. Xie, J.-P. McCreary, and R. Murtugudde, 2005: Impact of Indian Ocean sea surface temperature on developing El Niño. *J. Climate*, **18**, 302–319.
- Ashok, K., Z. Guan, and T. Yamagata, 2001: Impact of the Indian Ocean dipole on the relationship between the Indian monsoon rainfall and ENSO. *Geophys. Res. Lett.*, **28**, 4499–4502.
- Behera, S. K., J. J. Luo, S. Masson, P. Delecluse, S. Gualdi, and A. Navarra, 2005: Paramount impact of the Indian Ocean dipole on the east African short rains: A CGCM study. *J. Climate*, **18**, 4514–4530.
- Black, E., J. Slingo, and K. R. Sperber, 2003: An observational study of the relationship between excessively strong short rains in coastal east Africa and Indian Ocean SST. *Mon. Wea. Rev.*, **131**, 74–94.
- Cadet, D. L., 1985: The Southern Oscillation over the Indian Ocean. *J. Climatol.*, **5**, 189–212.
- Cai, W., H. H. Hendon, and G. Meyers, 2005: Indian Ocean dipolelike variability in the CSIRO Mark 3 coupled climate model. *J. Climate*, **18**, 1449–1468.
- Carton, J. A., G. Chepurin, X. Cao, and B. Giese, 2000: A simple ocean data assimilation analysis of the global upper ocean 1950–95. Part I: Methodology. *J. Phys. Oceanogr.*, **30**, 294–309.
- Clarke, A. J., and X. Liu, 1994: Interannual sea level in the northern and eastern Indian Ocean. *J. Phys. Oceanogr.*, **24**, 1224–1235.
- Davey, M. K., and Coauthors, 2002: STOIC: A study of coupled model climatology and variability in tropical ocean regions. *Climate Dyn.*, **18**, 403–420.
- Delworth, T., and Coauthors, 2006: GFDL's CM2 global coupled climate models. Part I: Formulation and simulation characteristics. *J. Climate*, **19**, 643–674.
- Deser, C., A. S. Phillips, and J. W. Hurrell, 2004: Pacific interdecadal climate variability: Linkages between the Tropics and North Pacific during boreal winter since 1900. *J. Climate*, **17**, 3109–3124.
- Diansky, N., and E. Volodin, 2002: Simulation of present-day climate with a coupled atmosphere–ocean general circulation model. *Izv. Atmos. Oceanic Phys.*, **38**, 732–747.
- Drosowsky, W., 1993: Potential predictability of winter rainfall over southern and eastern Australia using Indian Ocean sea-surface temperature anomalies. *Aust. Meteor. Mag.*, **42**, 1–6.
- England, M., C. C. Ummenhofer, and A. Santoso, 2006: Interannual rainfall extremes over southwest western Australia linked to Indian Ocean climate variability. *J. Climate*, **19**, 1948–1969.
- Fischer, A., P. Terray, E. Guilyardi, S. Gualdi, and P. Delecluse, 2005: Two independent triggers for the Indian Ocean dipole/zonal mode in a coupled GCM. *J. Climate*, **18**, 3428–3449.
- Flato, G., and G. Boer, 2001: Warming asymmetry in climate change simulations. *Geophys. Res. Lett.*, **28**, 195–198.
- Giannini, A., R. Saravanan, and P. Chang, 2003: Oceanic forcing of Sahel rainfall on interannual to interdecadal time scales. *Science*, **302**, 1027–1030.
- Goddard, L., and N. E. Graham, 1999: The importance of the Indian Ocean for simulating rainfall anomalies over eastern and southern Africa. *J. Geophys. Res.*, **104**, 19 099–19 116.
- Goosse, H., and T. Fichefet, 1999: Importance of ice–ocean interactions for the global ocean circulation: A model study. *J. Geophys. Res.*, **104**, 23 337–23 355.
- Gordon, C., C. Cooper, C. A. Senior, H. T. Banks, J. M. Gregory, T. C. Johns, J. F. B. Mitchell, and R. A. Wood, 2000: The simulation of SST, sea ice extents and ocean heat transports in a version of the Hadley Centre coupled model without flux adjustments. *Climate Dyn.*, **16**, 147–168.
- Gualdi, S. E., E. Guilyardi, A. Navarra, S. Masina, and P. Delecluse, 2003: The interannual variability in the Indian Ocean as simulated by a CGCM. *Climate Dyn.*, **20**, 567–582.
- Hoerling, M., J. Hurrell, T. Xu, G. T. Bates, and A. Phillips, 2004: Twentieth century North Atlantic climate change. Part II: Understanding the effect of Indian Ocean warming. *Climate Dyn.*, **23**, 391–405.
- Iizuka, S., T. Matsuura, and T. Yamagata, 2000: The Indian Ocean SST dipole simulated in a coupled general circulation model. *Geophys. Res. Lett.*, **27**, 3369–3372.
- Kiehl, J. T., and P. R. Gent, 2004: The Community Climate System Model, version 2. *J. Climate*, **17**, 3666–3682.
- Klein, S. A., B. J. Soden, and N. C. Lau, 1999: Remote sea surface temperature variations during ENSO: Evidence for a tropical atmospheric bridge. *J. Climate*, **12**, 917–932.
- Lareef, Z., A. S. Rao, and T. Yamagata, 2003: Modulation of Sri

- Lankan Maha rainfall by the Indian Ocean dipole. *Geophys. Res. Lett.*, **30**, 1063, doi:10.1029/2002GL015639.
- Latif, M., D. Dommenges, and M. Dima, 1999: The role of Indian Ocean sea surface temperature in forcing east African rainfall anomalies during December–January 1997/98. *J. Climate*, **12**, 3497–3504.
- Lau, N.-C., and M. J. Nath, 2004: Coupled GCM simulation of atmosphere–ocean variability associated with the zonally asymmetric SST changes in the tropical Indian Ocean. *J. Climate*, **17**, 245–265.
- Li, J., and A. J. Clarke, 2004: Coastline direction, interannual flow, and the strong El Niño currents along Australia's nearly zonal southern coast. *J. Phys. Oceanogr.*, **34**, 2373–2381.
- Meehl, G. A., J. M. Arblaster, and J. Loschnigg, 2003: Coupled ocean–atmosphere dynamical processes in the tropical Indian and Pacific Oceans and the TBO. *J. Climate*, **16**, 2138–2158.
- , W. Washington, W. Collins, J. Arblaster, A. Hu, L. Buja, W. Strand, and H. Teng, 2005: How much more global warming and sea level rise? *Science*, **307**, 1769–1772.
- Meyers, G., 1996: Variation of Indonesian throughflow and the El Niño–Southern Oscillation. *J. Geophys. Res.*, **101**, 12 255–12 263.
- Murtugudde, R. G., J. P. McCreary, and A. J. Busalacchi, 2000: Oceanic processes associated with anomalous events in the Indian Ocean with relevance to 1997–1998. *J. Geophys. Res.*, **105**, 3295–3306.
- Neelin, J. D., and Coauthors, 1998: ENSO theory. *J. Geophys. Res.*, **103**, 14 261–14 290.
- Nicholls, N., 1989: Sea surface temperatures and Australian winter rainfall. *J. Climate*, **2**, 965–973.
- Nigam, S., and H.-S. Shen, 1993: Structure of oceanic and atmospheric low-frequency variability over the tropical Pacific and Indian Oceans. Part I: COADS observations. *J. Climate*, **6**, 1750–1771.
- Nozawa, T., T. Nagashima, H. Shioyama, and S. A. Crooks, 2005: Detecting natural influence on surface air temperatures change in the early twentieth century. *Geophys. Res. Lett.*, **23**, L20719, doi:10.1029/2005GL023540.
- Okumuara, Y., and S.-P. Xie, 2004: Interaction of the Atlantic equatorial cold tongue and African monsoon. *J. Climate*, **17**, 3588–3601.
- Pan, H. Y., and A. H. Oort, 1983: Global climate variations associated with sea surface temperature anomalies in the eastern equatorial Pacific Ocean for the 1958–1973 period. *Mon. Wea. Rev.*, **111**, 1244–1258.
- Perigaud, C., and J. McCreary, 2003: Influence of interannual rainfall anomalies on sea level variations in the tropical Indian Ocean. *J. Geophys. Res.*, **108**, 3335, doi:10.1029/2003JC001857.
- Potemra, J. T., 2001: The potential role of equatorial Pacific winds on southern tropical Indian Ocean Rossby waves. *J. Geophys. Res.*, **106**, 2407–2422.
- Qu, T., and G. Meyers, 2005: Seasonal variation of barrier layer in the southeastern tropical Indian Ocean. *J. Geophys. Res.*, **110**, C11003, doi:10.1029/2004JC002816.
- Rao, A. S., S. K. Behera, Y. Masumoto, and T. Yamagata, 2002: Interannual variability in the subsurface tropical Indian Ocean. *Deep-Sea Res.*, **49B**, 1549–1572.
- Rao, S., and T. Yamagata, 2004: Abrupt termination of Indian Ocean dipole events in response to intraseasonal disturbances. *Geophys. Res. Lett.*, **31**, L19306, doi:10.1029/2004GL020842.
- , and S. Behera, 2005: Subsurface influence on SST in the tropical Indian Ocean: Structure and interannual variability. *Dyn. Atmos. Oceans*, **39**, 103–135.
- Rayner, N. A., D. E. Parker, P. Frich, E. B. Horton, C. K. Folland, and L. V. Alexander, 2000: SST and sea-ice fields for ERA40. *Proc. Second WCRP Int. Conf. on Reanalyses*, Reading, United Kingdom, WCRP-109, WMO/TD-No. 985, 18–21.
- Reynolds, R. W., and T. M. Smith, 1994: Improved global sea surface temperature analyses using optimum interpolation. *J. Climate*, **7**, 929–948.
- Russell, G., J. Miller, and D. Rind, 1995: A coupled atmosphere–ocean model for transient climate change studies. *Atmos.–Ocean*, **33**, 683–730.
- Saji, N. H., and T. Yamagata, 2003a: Possible impacts of Indian Ocean Dipole mode events on global climate. *Climate Res.*, **25**, 151–169.
- , and —, 2003b: Structure of SST and surface wind variability during Indian Ocean dipole mode years: COADS observations. *J. Climate*, **16**, 2735–2751.
- , B. N. Goswami, P. N. Vinayachandran, and T. Yamagata, 1999: A dipole mode in the tropical Indian Ocean. *Nature*, **401**, 360–363.
- , T. Ambrizzi, and S. Simone, 2005a: Indian Ocean Dipole mode events and austral surface temperature anomalies. *Dyn. Atmos. Oceans*, **39**, 87–101.
- Schmidt, G., and Coauthors, 2006: Present-day atmospheric simulations using GISS ModelE: Comparison to in situ, satellite, and reanalysis data. *J. Climate*, **19**, 153–192.
- Shinoda, T., H. H. Hendon, and M. A. Alexander, 2004: Surface and subsurface dipole variability in the Indian Ocean and its relation with ENSO. *Deep-Sea Res.*, **51**, 619–635.
- Spencer, H., R. Sutton, J. Slingo, M. Roberts, and E. Black, 2005: Indian Ocean climate and dipole variability in Hadley Centre coupled GCMs. *J. Climate*, **18**, 2286–2307.
- Timmermann, A. J., J. Oberhuber, A. Bacher, M. Esch, M. Latif, and E. Roeckner, 1999: Increased El Niño frequency in a climate model forced by future greenhouse warming. *Nature*, **398**, 694–697.
- Venzke, S., M. Latif, and A. Villwock, 2000: The coupled GCM ECHO-2. Part II: Indian Ocean response to ENSO. *J. Climate*, **13**, 1371–1387.
- Verschell, M. A., J. C. Kindle, and J. J. O'Brien, 1995: Effects of Indo-Pacific throughflow on the upper tropical Pacific and Indian Oceans. *J. Geophys. Res.*, **100**, 18 409–18 420.
- Wajswicz, R. C., 2005: Forecasting extreme events in the tropical Indian Ocean sector climate. *Dyn. Atmos. Oceans*, **39**, 137–151.
- Wang, B., R. Wu, and T. Li, 2003: Atmosphere–warm ocean interaction and its impact on Asian–Australian monsoon variability. *J. Climate*, **16**, 1195–1211.
- Webster, P. J., A. M. Moore, J. P. Loschnigg, and R. R. Leben, 1999: Coupled ocean–atmosphere dynamics in the Indian Ocean during 1997–98. *Nature*, **401**, 356–360.
- Wijffels, S., and G. Meyers, 2004: An intersection of oceanic waveguides: Variability in the Indonesian throughflow region. *J. Phys. Oceanogr.*, **34**, 1232–1253.
- Wu, R., and B. P. Kirtman, 2004: Understanding the impacts of the Indian Ocean on ENSO in a coupled GCM. *J. Climate*, **17**, 4019–4031.
- Xie, P., and P. A. Arkin, 1996: Analyses of global monthly precipitation using gauge observations, satellite estimates, and numerical model predictions. *J. Climate*, **9**, 840–858.
- Xie, S.-P., Y. Tanimoto, H. Noguchi, and T. Matsuno, 1999: How

- and why climate variability differs between the tropical Pacific and the Atlantic. *Geophys. Res. Lett.*, **26**, 1609–1612.
- , H. Annamalai, F. A. Schott, and J. P. McCreary, 2002: Structure and mechanisms of south Indian Ocean climate variability. *J. Climate*, **15**, 864–878.
- Yamagata, T., S. K. Behera, J. J. Luo, S. Masson, M. R. Jury, and S. A. Rao, 2004: Coupled ocean–atmosphere variability in the tropical Indian Ocean. *Earth Climate: The Ocean–Atmosphere Interaction, Geophys. Monogr.*, Vol. 147, Amer. Geophys. Union, 189–212.
- Yu, J. Y., C. R. Mechoso, J. C. McWilliams, and A. Arakawa, 2002: Impacts of Indian Ocean on ENSO cycles. *Geophys. Res. Lett.*, **29**, 1204, doi:10.1029/2001GL014098.
- Yu, Y., X. Zhang, and Y. Guo, 2004: Global coupled ocean–atmosphere general circulation models in LASG/IAP. *Adv. Atmos. Sci.*, **21**, 444–455.
- Yukimoto, S., and Coauthors, 2001: The New Meteorological Research Institute coupled GCM (MRI–CGCM2)—Model climate and variability. *Pap. Meteor. Geophys.*, **51**, 47–88.
- Yulaeva, E., and J. M. Wallace, 1994: The signature of ENSO in global temperature and precipitation fields derived from the Microwave Sounding Unit. *J. Climate*, **7**, 1719–1736.